Chinese Chemical Letters 34 (2023) 108572

Contents lists available at ScienceDirect

Chinese Chemical Letters

journal homepage: www.elsevier.com/locate/cclet

Ethylene glycol-regulated ammonium vanadate with stable layered structure and favorable interplanar spacing as high-performance cathode for aqueous zinc ion batteries

Chao Lu[a,b], Zhi Yang[a], Yujie Wang[b,*], Yun Zhang[c], Hao Wu[c], Yi Guo[d], Wenlong Cai[c,*]

[a] School of Mechanical Engineering, Chengdu University, Chengdu 610106, China
[b] Department of Chemistry, College of Resource and Environment, Baoshan University, Baoshan 678000, China
[c] College of Materials Science and Engineering, Sichuan University, Chengdu 610064, China
[d] College of Optoelectronic Engineering, Chengdu University of Information Technology, Chengdu 610225, China

ARTICLE INFO

Article history:
Received 11 April 2023
Revised 5 May 2023
Accepted 11 May 2023
Available online 17 May 2023

Keywords:
Ammonium vanadate rods
Ethylene glycol reduction
Zn^{2+} storage
Cathode
Aqueous zinc ion battery

ABSTRACT

Ammonium vanadate compounds featuring large capacity, superior rate capability and light weight are regarded as promising cathode materials for aqueous zinc ion batteries (AZIBs). However, the controllable synthesis of desired ammonium vanadates remains a challenge. Herein, various ammonium vanadate compounds were successfully prepared by taking advantage of ethylene glycol (EG) regulated polyol-reduction strategy and solvent effect *via* hydrothermal reaction. The morphology and crystalline phase of resultant products show an evolution from dendritic $(NH_4)_2V_6O_{16}$ to rod-like $NH_4V_4O_{10}$ and finally to lamellar $(NH_4)_2V_4O_9$ as increasing the amount of EG. Specifically, the $NH_4V_4O_{10}$ product exhibits a high initial capacity of 427.5 mAh/g at 0.1 A/g and stable cycling with a capacity retention of 90.4% after 5000 cycles at 10 A/g. The relatively excellent electrochemical performances of $NH_4V_4O_{10}$ can be ascribed to the stable open-framework layered structure, favorable (001) interplanar spacing, and peculiar rod-like morphology, which are beneficial to the highly reversible Zn^{2+} storage behaviors. This work offers a unique way for the rational design of high-performance cathode materials for AZIBs.

Due to the increasing resource consumption and environmental pollution, it is urgent to develop clean and safe energy storage devices [1,2]. In recent years, aqueous zinc ion batteries (AZIBs) with features of abundant resource, low cost, high safety, and environmental friendliness, have shown a great potential to substitute commercial lithium ion batteries in the field of large-scale energy storage [3–5]. However, the practical application of AZIBs has been hindered by the lack of high-performance cathode materials [6]. As a result, several kinds of cathodes including Mn-based oxides [7,8], V-based compounds [9,10], Prussian blue analogues [11], polyanionic compounds [12], and sulphides [13], have been explored as cathodes for AZIBs. It is worth noting that most of these cathode materials do not perform well enough in terms of cycle performance, rate capability, and/or discharge capacity [14,15]. Particularly, open-framework layered-type V-based materials consisting of zinc vanadate [16], sodium vanadate [17], potassium vanadate [18], and ammonium vanadate [19], have been extensively studied on account of their tunable interlayer spacing and multistep redox reactions. Among them, the family of ammonium vanadates has been considered as promising cathodes for AZIBs due to the inherent merits of light weight resulting in higher gravimetric capacity, and robust hydrogen bonds (N–H···O) between NH_4^+ and V-O layer contributing to better structural stability. Furthermore, the reversible insertion/extraction of Zn^{2+} (0.76 Å) with a smaller ionic radius than that of NH_4^+ (1.43 Å) supporting the V-O layers can be achievable during the charge-discharge process, enabling the fast diffusion of Zn^{2+} ions.

Currently, the hydrothermal method as an effective and facile approach has been primarily implemented to prepare ammonium vanadates [20], displaying distinct advantages of low reaction temperature, easily controllable morphology, and exemption from further calcination. In spite of some virtues brought by the hydrothermal technique using water as the solvent, the resultant products yet suffer from a time-consuming process and large particle size owing to the small viscosity, high fluidity, and large interface tension of water which can lead to difficult control of reactant diffusion in different directions [21]. To tackle these issues, several studies have shown that adding viscous organic-solvent ethylene glycol (EG) [22–24] into an aqueous solution is favorable to in-

* Corresponding authors.
E-mail addresses: wangyujieufo@163.com (Y. Wang), caiwl@scu.edu.cn (W. Cai).

https://doi.org/10.1016/j.cclet.2023.108572
1001-8417/

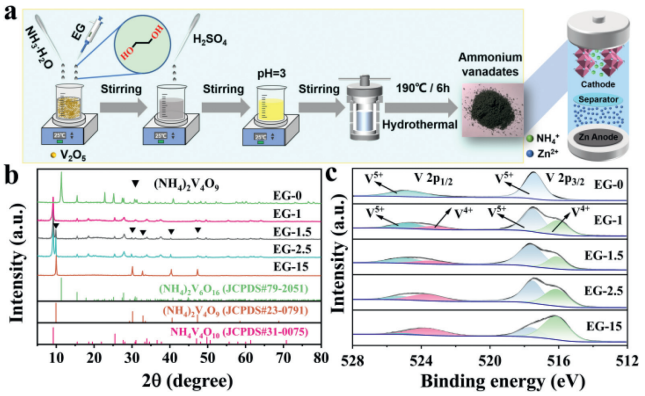

Fig. 1. (a) Synthetic procedure of ammonium vanadates. (b) XRD patterns and (c) V 2p XPS spectra of various samples.

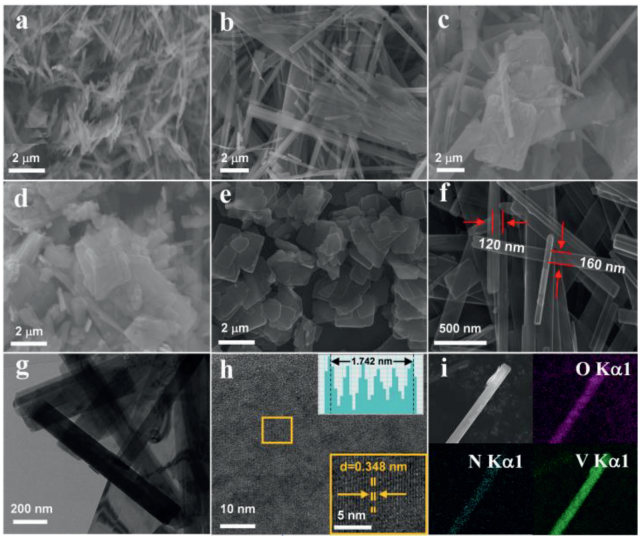

Fig. 2. SEM images of (a) EG-0, (b) EG-1, (c) EG-1.5, (d) EG-2.5, and (e) EG-15. (f) SEM, (g) TEM, (h) HRTEM images, and (i) elemental mappings of EG-1.

creasing the viscosity of the mixed solution, lowering the solubility of precursors, and controlling the nucleation and growth of grain to obtain the desired particle size distribution, morphology and electrochemical performance as well as shortened reaction time. For example, the prepared uniform rice grain-like $LiFePO_4$/C composites after introducing EG during the synthetic process could exhibit an initial discharge capacity of 155 mAh/g at a current density of 0.1 C as well as maintain 91.6% capacity retention after 100 cycles [21]. In addition, Guo and cooperators have revealed that EG adsorbing on the specific crystalline plane could drive the crystal growth in a definite direction, ultimately endowing the resulting $LiFePO_4$ nanoplates with the special morphology for facilitating the diffusion of lithium ions [25]. Accordingly, utilizing EG as a viscous organic solvent to construct the anticipant ammonium vanadate cathodes for AZIBs may be an ingenious and feasible route to address such aforementioned shortcomings.

More importantly, EG containing multi–hydroxyl groups can also act as a nontoxic, pollution-free, and low-cost reducing agent to obtain the specific crystalline phase under the conditions of high temperature and saturated vapor pressure in a sealed reactor. Inspired by these intriguing features of EG, it can be rationally inferred that the species of vanadium ions with multiple changeable valence states in ammonium vanadate compounds can be modulated by EG during the hydrothermal reaction, thus obtaining various ammonium vanadates. Moreover, for all we know, there have been few reports on the synthesis of ammonium vanadate compounds by EG regulating.

Thereby, in this work, for the first time, we synthesized various ammonium vanadate compounds with different morphologies and crystalline structures by an EG-regulated facile hydrothermal route combining polyol reduction strategy with the solvent effect of EG. The influences of EG addition amount on the synthesis of ammonium vanadates were systematically discussed. Compared with other products, the synthesized rod-like $NH_4V_4O_{10}$ cathode material can deliver a relatively high specific capacity of up to 427.5 mAh/g at a current density of 0.1 A/g and achieve excellent cycling stability over 5000 cycles even at 10 A/g. The investigation of the electrochemical mechanism gives further insight into the optimal performances based on the stable layered structure and larger (001) interplanar spacing. Such a facile and cost-effective strategy could light the practical application of AZIBs.

Firstly, a series of ammonium vanadates, named as EG-0, EG-1, EG-1.5, EG-2.5 and EG-15, were synthesized using a modified hydrothermal approach by adding different amounts of EG (0, 1, 1.5, 2.5 and 15 mL, respectively), as described in Fig. 1a and Experimental section in Supporting information. Interestingly, the crystalline phases of obtained products are sharply distinguishable, indicating the significant role of reduction ability of EG in the hydrothermal reaction. Observation from XRD patterns (Fig. 1b) clearly displays that pure $NH_4V_4O_{10}$ could be synthesized while adding a proper amount (~1 mL) of EG. By contrast, the hydrothermal product without adding EG could be synthesized by simply converting V_2O_5 and $NH_3 \cdot H_2O$ into pure $(NH_4)_2V_6O_{16}$. Moreover, it can be found that the valence state of V has also been changed. As depicted in the XPS spectra of V 2p (Fig. 1c), these peaks appearing at about 517.4 eV (V $2p_{3/2}$) and 524.7 eV (V $2p_{1/2}$) for $(NH_4)_2V_6O_{16}$ are attributed to V^{5+} [26,27]. However, the deconvoluted lower-energy bands of V^{4+} are ever-strengthening along with the increase of EG addition, indicating that more V^{5+} could be reduced to $V^{4+}$by EG, in line with the XRD results which show the growing intensity of characteristic peaks belonged to $(NH_4)_2V_4O_9$ with the increase of EG from 1.5 to 2.5 mL. Specially, with the addition of sufficient EG (15 mL), sole crystallized $(NH_4)_2V_4O_9$ can be formed owing to the complete reduction of V^{5+} ions into V^{4+} ions by EG additive (Figs. 1b and c). Additionally, it is worth noting that the small amounts of V^{5+} in EG-15 can be ascribed to the V^{4+} oxidation when exposed to air [28].

Importantly, $NH_4V_4O_{10}$ composed of VO_6 octahedra has exclusive single-connected oxygen atoms on the V-O layers which could afford strong interactions with NH_4^+ ions acting as strong "pillars" to strengthen the structure stability [29]. Nevertheless, $(NH_4)_2V_6O_{16}$ consisting of VO_5 square pyramids and VO_6 octahedra [30] as well as $(NH_4)_2V_4O_9$ built up of VO_4 tetrahedra and VO_5 square pyramids [31] own the undesired tri-connected oxygen atoms in the layered structure, which presents weak interactions with NH_4^+ ions to result in an unstable structure. Furthermore, $NH_4V_4O_{10}$ is endowed with larger (001) interplanar spacing of 9.6 Å than those of $(NH_4)_2V_6O_{16}$ (7.8 Å) and $(NH_4)_2V_4O_9$ (8.9 Å), being conducive to fast Zn^{2+} diffusion and vast Zn^{2+} storage sites for achievements of superior rate capability and high discharge capacity.

The morphology and microstructure characteristics of various samples were investigated by SEM and TEM observations. As exhibited in Figs. 2a-g and Fig. S1 (Supporting information), EG-0 has a dendritic structure (Fig. 2a), while EG-1 shows a defined rod-like structure with a diameter of about 120–160 nm (Figs. 2b, f and g), demonstrating the evident impact of EG addition in terms of preferential growth of ammonium vanadate compounds. The lamellar structure could be evolved apparently as increasing EG

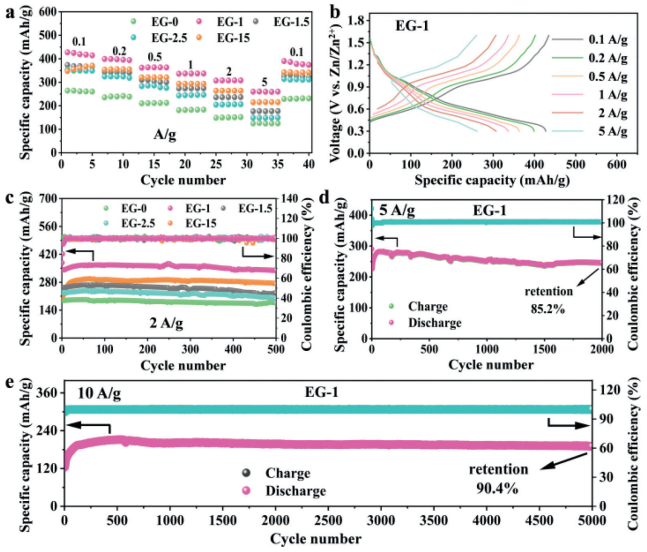

Fig. 3. (a) Rate performances, (b) charge/discharge curves for EG-1. (c) Cycling stability at 2 A/g. Cycling stability at current densities of (d) 5 A/g and (e) 10 A/g for EG-1.

(Figs. 2c and d). In particular, the EG-15 sample shows a thorough lamellar morphology (Fig. 2e). The morphology evolution mechanism could be reasonably elucidated that EG as a viscous organic solvent cannot only regulate the nucleation and growth of grains, as well as ameliorate the size and homogeneity of crystals [32], but also increase the solution viscosity, decrease the precursor solubility and ion diffusion rate in the solution [33]. Thus, excessive EG would seriously slow the axial growth rate, resulting in the dendritic structure evolving into a lamellar structure. The substantial gaps originating from rod stacking of EG-1 not only facilitate electrolyte penetration to increase the contact area between electrolyte and $NH_4V_4O_{10}$ electrode, but also provide abundant active sites for zinc ion storage [34,35]. Furthermore, HRTEM images (Fig. 2h) show that the lattice spacing of 0.348 nm matches well with the (110) facet of monoclinic $NH_4V_4O_{10}$. In addition, EDS results (Fig. 2i) display that N, V, and O elements are uniformly distributed throughout the whole rod of EG-1.

To explore the electrochemical properties of these ammonium vanadates as cathodes, aqueous Zn//ammonium vanadates cells were assembled. Fig. 3a shows the rate capabilities of five samples at various current densities from 0.1 A/g to 5 A/g. Due to the larger ion diffusion channel, EG-1 can deliver higher discharge capacities (427.5, 399.2, 362.1, 336.4, 307.2 and 260.6 mAh/g at 0.1, 0.2, 0.5, 1, 2 and 5 A/g, respectively) than the remaining four samples, comparable to or even better than other reported cathodes for AZIBs listed in Table S1 (Supporting information). Besides, the specific capacity of EG-1 with a more stable crystal structure could still recover to 390.2 mAh/g as the current density returns to 0.1 A/g, exhibiting a high recovery rate of 91.3%. The corresponding GCD curves in Fig. 3b also confirm the excellent electrochemical performance. In spite of capacity fading with the increase of current density, all the GCD curves still have a similar shape and possess multiple voltage plateaus, suggesting that the insertion/extraction process of Zn^{2+} concerns a highly reversible multi-step electrochemical reaction.

What is more, Fig. 3c and Fig. S2 (Supporting information) exhibit the comparisons of cycling performances and corresponding GCD curves at the current densities from 0.1 A/g to 2 A/g. Visibly, the samples with adding EG reveal more excellent cycling stability than EG-0. Intriguingly, the initial discharge capacity of EG-1 can reach as high as 378.7 mAh/g at 0.5 A/g and still maintain a capacity of 361.2 mAh/g with a retention rate of 95.4% after 50 cycles, better than those of EG-1.5 and EG-2.5. Additionally, the maximum discharge capacity of EG-1 at 2 A/g reaches a higher 372.8 mAh/g than those of EG-0, EG-1.5, EG-2.5, and EG-15. Even after 500 cycles, EG-1 can still retain a discharge capacity of 340.2 mAh/g. The outstanding performances of EG-1 could be attributed to the existing gap structure of stacked rods affording sufficient solid/liquid contact as well as plentiful active sites. Moreover, it is found that EG-1 requires fewer than 40 cycles to reach the maximum specific capacity compared with 55 cycles for EG-1.5 and 60 cycles for EG-2.5, manifesting the faster activation process of EG-1 [36–38]. The fastest activation process for EG-1 can be ascribed to the favorable rod-like morphology affording abundant active sites and convenient diffusion channels for Zn^{2+} insertion/extraction, enabling the achievement of reduced polarization and enhanced kinetics. Excitingly, EG-1 benefiting the structure stability from its exclusive single-connected oxygen atoms on the V-O layers can also keep a capacity retention of 85.2% after 2000 cycles at 5 A/g, and even retains an ultra-high specific capacity of 191.4 mAh/g with 90.4% retention after undergoing 5000 loops at 10 A/g (Figs. 3d and e).

To dig a deep insight into the evolution of crystal structure for EG-1 during the electrochemical process, the *ex-situ* XRD tests were performed at different charge/discharge voltages in the 2nd cycle at 0.1 A/g (Fig. S3a in Supporting information). As shown in the corresponding XRD patterns (Figs. S3b and c in Supporting information), the diffraction peak at about 9.2° assigned to the (001) facet of $NH_4V_4O_{10}$ shows a significant swing due to the repeated insertion/extraction of Zn^{2+} between V-O layers [39], indicating the contraction/expansion of layer spacing which mainly arises from the variable electrostatic repulsion between O^{2-} ions in the adjacent layers [20,29,40]. The *ex-situ* XPS spectra of Zn 2p and O 1s for EG-1 at different states have been exhibited in Fig. S4 (Supporting information). When firstly discharged to 0.3 V and then charged to 1.6 V, the initial enhancement and subsequent attenuation of Zn^{2+} signal further confirm the Zn^{2+} insertion/extraction in V-O layers. The significantly strengthened peak of crystal water after discharging to 0.3 V implies that H_2O molecules are also intercalated into the V-O layers. Furthermore, HRTEM images of EG-1 after charging and discharging (Fig. S5 in Supporting information) also reveal that the corresponding interlayer spacing of the (110) crystal plane is 0.347 nm when discharged to 0.3 V, but achieves 0.352 nm while charged to 1.6 V. Hence, the structural evolution mechanism of $NH_4V_4O_{10}$ (Fig. S6 in Supporting information) can be proposed that Zn^{2+} and H_2O would enter into V-O layers to form $Zn_mNH_4V_4O_{10}\cdot xH_2O$ and $Zn_3(OH)_2V_2O_7\cdot 2H_2O$ (JCPDS No. 50–0570) along with the gradual voltage drop, whereas strip out during the gradual increase of voltage accompanying with $Zn_3(OH)_2V_2O_7\cdot 2H_2O$ disappearing to obtain $Zn_nNH_4V_4O_{10}\cdot yH_2O$ [16,29,41]. During the discharging process, the presence of $Zn_3(OH)_2V_2O_7\cdot 2H_2O$ byproduct is probably ascribed to the side reactions of V-O layers with Zn^{2+} ions, co-intercalated H_2O molecules and OH^-groups in aqueous electrolyte [42].

The merits originated from the interesting structural evolution of $NH_4V_4O_{10}$ during the charge/discharge process provoke the motivation for exploring its electrochemical properties as cathode material for AZIBs. Fig. 4a displays the CV curves of EG-1 within the voltage window from 0.3 V to 1.6 V at a scan rate of 0.1 mV/s, where the redox peaks near 1.12/0.96 and 0.56/0.43 V correspond to the redox reactions of V^{5+}/V^{4+} and V^{4+}/V^{3+} [43]. In addition, the redox peaks at 1.43/1.32 V represent a reversible electrochemical reaction for the formation and decomposition of $Zn_3(OH)_2V_2O_7\cdot 2H_2O$ [44], which can be also confirmed by the emergence and vanish of $Zn_3(OH)_2V_2O_7\cdot 2H_2O$ phase when the pristine EG-1 is firstly discharged to 0.3 V and then charged to 1.6 V (see the *ex-situ* XRD patterns in Fig. S3b). The reduction

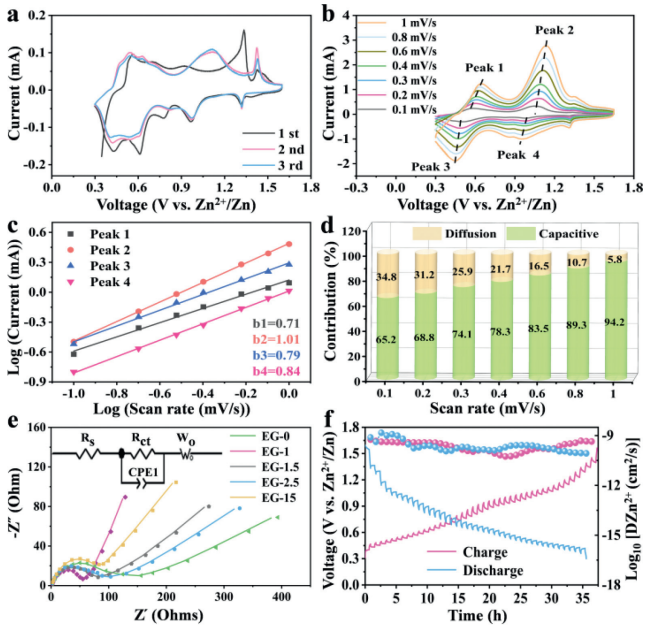

Fig. 4. (a) CV curves at a scan rate of 0.1 mV/s, (b) CV curves at different scan rates, (c) plots of log(i) versus log(v), (d) capacitive contributions at different scan rates for EG-1. (e) Nyquist plots after 50 cycles (inset is the equivalent circuit model). (f) GITT curves and ion diffusion coefficients of EG-1.

peak that appears at near 0.8 V is associated with the entry of H_2O into V-O layers [45]. It is noteworthy that the potential differences between each pair of redox peaks are small as well as the same-type peak areas are very close, demonstrating the excellent electrochemical stability. Moreover, all CV curves are highly overlapping except the first cycle, hinting at good reversibility of Zn^{2+} insertion/extraction [46]. In addition, several platforms exhibited in the GCD curves (Fig. S7a in Supporting information) can also verify the multiple insertion/deinsertion process of Zn^{2+}.

To further investigate the Zn^{2+}ion diffusion kinetics, CV tests were performed on all five samples at different scan rates from 0.1 mV/s to 1 mV/s. Observations from Fig. 4b and Figs. S8a, d, g and j (Supporting information) show the slight shift of the redox peaks due to polarization effect [47]. The similar shape of CV curves toward overall scan rates indicates the remarkable electrochemical stability for EG-1 during the insertion/extraction of Zn^{2+} [48]. Moreover, the zinc-storage behavior can be determined based on the measured current and scan rate *via* the equation: $i = av^b$, where i is the peak current, v represents the scan rate, as well as a and b are variable parameters. Generally, the b value ranges from 0.5 to 1.0, where $b = 0.5$ suggests a diffusion-controlled process while $b = 1$ represents a completely surface-controlled capacitive process. Depending on the formula: $\log(i) = b\log(v) + \log(a)$, the calculated b-values for EG-1 are 0.71, 1.01, 0.79 and 0.84, respectively (Fig. 4c). Thus, it illustrates that EG-1 has the dominated Zn^{2+} storage mechanism of capacitive behavior and displays an obvious advantage over other four samples (Figs. S8b, e, h and k in Supporting information). In addition, the capacitive contribution can be calculated by the equation: $i = k_1v + k_2v^{1/2}$, where k_1v means the surface capacitive contribution, and $k_2v^{1/2}$ represents the diffusion-controlled proportion. As shown in Fig. S7b (Supporting information), EG-1 has a capacitive contribution of up to 83.5% at a scan rate of 0.6 mV/s (light green shaded area). A more intuitive capacitance contribution is displayed in Fig. 4d, of which the capacitive contribution rate increases from 65.2 to 94.2% with increasing scan rate, much higher than those of EG-0, EG-1.5, EG-2.5 and EG-15 (Figs. S8c, f, i and m in Supporting information). To this end, the favorable capacitive behavior could endow EG-1 with excellent electrochemical properties, especially the high-rate capability [49], thereby greatly facilitating the reversible Zn^{2+} intercalation/deintercalation.

Furthermore, electrochemical impedance spectroscopy (EIS) tests were applied to evaluate the electrode resistance of EG-1. As shown in Fig. 4e, EIS curves of all samples consist of a semicircle representing charge transfer resistance (R_{ct}) and a slope line referring to ion diffusion in the high and low frequency regions, respectively [50,51]. Evidently, the R_{ct} of EG-1 (53.3 Ω) is smaller than those of EG-0 (151.9 Ω), EG-1.5 (87.8 Ω), EG-2.5 (100.4 Ω), and EG-15 (80.7 Ω), indicating faster charge transfer properties. Meanwhile, Fig. S9 (Supporting information) also unfolds the fitting results for Z'-$\omega^{-1/2}$ in the low frequency region, where the slope of EG-1 is lower than those of other samples, verifying the superior Zn^{2+}diffusion ability for EG-1.

Additionally, five samples were subjected to galvanostatic intermittent titration technique (GITT) measurements to further survey the corresponding Zn^{2+} diffusion coefficients ($D_{Zn^{2+}}$) according to the equation [52]:

$$D_{Zn^{2+}} = \frac{4}{\pi\tau}\left(\frac{m_B V_M}{M_B S}\right)^2\left(\frac{\Delta E_s}{\Delta E_t}\right)^2 \quad (1)$$

where M_B and m_B represent the molecular weight and mass of active material, respectively, V_M and S are the molar volume and surface area of active material, respectively. ΔE_s and ΔE_t stand for the change of steady-state voltage and total charge of cell voltage during the current pulse, respectively, and τ is the relaxation time. Fig. 4f shows the GITT curves and the corresponding $D_{Zn^{2+}}$ under the test conditions in Fig. S10 (Supporting information). Accordingly, the calculated $D_{Zn^{2+}}$ values of EG-1 during insertion and extraction have a relatively small difference and range from 1.48×10^{-9} cm^2/s to 5.54×10^{-11} cm^2/s, higher than those of EG-0, EG-1.5, EG-2.5 and EG-15 ranging from 4.55×10^{-10} cm^2/s to 7.7×10^{-12} cm^2/s, 3.71×10^{-10} cm^2/s to 6.72×10^{-12} cm^2/s, 5.67×10^{-11} cm^2/s to 2.21×10^{-12} cm^2/s, and 3.61×10^{-10} cm^2/s to 1.82×10^{-11} cm^2/s, respectively (Fig. S11 in Supporting information). Thereby, combing excellent capacitive contribution with lower R_{ct}, it could conclude that EG-1 can not only perform rapid ion diffusion, but also maintain high electrochemical stability during cycling.

In summary, various ammonium vanadates have been successfully fabricated through a facile hydrothermal method by regulating the amount of EG. The reduction ability and solvent effect from EG make a crucial impact on the morphology, phase composition and electrochemical properties of the synthetic products. Significantly, $NH_4V_4O_{10}$ with adding 1 mL EG has been proven to be a desirable cathode material for AZIBs in view of its favorable open-framework layered structure with excellent stability and large (001) interplanar spacing as well as the peculiar rod-like morphology contributing to favorable zinc ion diffusion, thus exhibiting the high initial capacity (427.5 mAh/g at 0.1 A/g), superior rate behavior (discharge capacity of 260.6 mAh/g at 5 A/g), and long-periodic cycle life (90.4% capacity retention after 5000 cycles at 10 A/g). This work provides an important direction for rationally designing advanced cathode materials for AZIBs by tailoring the morphology and crystalline structure of vanadates based on EG-regulated polyol reduction strategy and solvent effect.

Declaration of competing interest

The authors declare that they have no known competing financial interests or personal relationships that could have appeared to influence the work reported in this paper.

Acknowledgments

This work was supported by the National Natural Science Foundation of China (No. 22005172), Natural Science Foundation of Sichuan Province (No. 2023NSFSC1124), Yunnan Fundamental Research Projects (No. 202201AU070151).

Supplementary materials

Supplementary material associated with this article can be found, in the online version, at doi:10.1016/j.cclet.2023.108572.

References

[1] J. Lee, A. Urban, X. Li, et al., Science 343 (2014) 519–522.
[2] L. Wang, J.L. Shi, H. Su, et al., Small 14 (2018) 1800887.
[3] M. Hu, X. Pang, Z. Zhou, J. Power Sources 237 (2013) 229–242.
[4] Y. Niu, D. Wang, Y. Ma, et al., Chin. Chem. Lett. 33 (2022) 1430–1434.
[5] X. Zhang, H. Luo, Y. Guo, et al., Chem. Eng. J. 457 (2023) 141305.
[6] A. Kwade, W. Haselrieder, R. Leithoff, et al., Nat. Energy 3 (2018) 290–300.
[7] C. Zhu, G. Fang, S. Liang, et al., Energy Storage Mater. 24 (2020) 394–401.
[8] H. Yang, T. Zhang, D. Chen, et al., Adv. Mater. (2023) 2300053.
[9] X. Li, H. Cheng, H. Hu, et al., Chin. Chem. Lett. 32 (2021) 3753–3761.
[10] C. Lu, Z. Yang, Y. Ding, et al., Mater. Today Commun. 35 (2023) 105993.
[11] H. Yi, R. Qin, S. Ding, et al., Adv. Funct. Mater. 31 (2020) 2006970.
[12] Y. Lan, W. Yao, X. He, et al., Angew. Chem. Int. Ed. 59 (2020) 9255–9262.
[13] Z. Yang, B. Wang, Y. Chen, et al., Natl. Sci. Rev. 10 (2022) nwac268.
[14] Y. Zhang, E.H. Ang, K.N. Dinh, et al., Mater. Chem. Front. 5 (2021) 744–762.
[15] H. Tang, Z. Peng, L. Wu, et al., Electrochem. Energy Rev. 1 (2018) 169–199.
[16] D. Kundu, B.D. Adams, V. Duffort, et al., Nat. Energy 1 (2016) 1–8.
[17] D. Xie, F. Hu, X. Yu, et al., Chin. Chem. Lett. 31 (2020) 2268–2274.
[18] L.W. Dong, R.G. Xu, P.P. Wang, et al., J. Power Sources 479 (2020) 228793.
[19] F. Hu, Y. Gu, F. Cui, et al., Chin. Chem. Lett. 32 (2021) 3793–3798.
[20] C. Huang, S. Liu, J. Feng, et al., J. Power Sources 490 (2021) 229528.
[21] Y. Li, J. Wang, J. Yao, et al., Mater. Chem. Phys. 224 (2019) 293–300.
[22] H.C. Liu, Y.M. Wang, C.C. Hsieh, Ceram. Int. 43 (2017) 3196–3201.
[23] H. Ghafarian-Zahmatkesh, M. Javanbakht, M. Ghaemi, J. Power Sources 284 (2015) 339–348.
[24] X. Tang, R.Y. Hong, W.G. Feng, et al., J. Alloys Compd. 562 (2013) 211–218.
[25] H. Guo, Y. Liu, Y. Xi, et al., Solid State Ion. 298 (2016) 44–50.
[26] H. Fei, X. Wu, H. Li, et al., J. Colloid Interface Sci. 415 (2014) 85–88.
[27] J. Mendialdua, R. Casanova, Y. Barbaux, J. Electron. Spectrosc. Relat. Phenom. 71 (1995) 249–261.
[28] F. Cui, F. Hu, X. Yu, et al., J. Power Sources 492 (2021) 229629.
[29] B. Tang, J. Zhou, G. Fang, et al., J. Mater. Chem. A 7 (2019) 940–945.
[30] L. Xu, Y. Zhang, H. Jiang, et al., Colloids Surf. A 593 (2020) 124621.
[31] Y. Zhang, H. Jiang, L. Xu, et al., ACS Appl. Energy Mater. 2 (2019) 7861–7869.
[32] U. Jeong, Y. Wang, M. Ibisate, et al., Adv. Funct. Mater. 15 (2005) 1907–1921.
[33] H. Astaraki, S. Masoudpanah, S. Alamolhoda, J. Mater. Res. Technol. 14 (2021) 229–241.
[34] Y. Cao, C. Liu, M. Wang, et al., Energy Storage Mater. 29 (2020) 207–215.
[35] H. Liu, X. Liang, T. Jiang, et al., Sol. Energy Mater. Sol. Cells 238 (2022) 111627.
[36] K. Zhou, S. Wang, S. Zhang, et al., J. Mater. Chem. A 8 (2020) 14031–14042.
[37] Y. Tao, Z. Li, L. Tang, et al., Electrochim. Acta 331 (2020) 135296.
[38] D. He, Y. Peng, Y. Ding, et al., J. Power Sources 484 (2021) 229284.
[39] F. Zhang, X. Sun, M. Du, et al., Energy Environ. Mater. 4 (2021) 620–630.
[40] B. Tang, G. Fang, J. Zhou, et al., Nano Energy 51 (2018) 579–587.
[41] X. Guo, G. Fang, W. Zhang, et al., Adv. Energy Mater. 8 (2018) 1801819.
[42] Q. Zong, W. Du, C. Liu, et al., Nano Micro Lett. 13 (2021) 116.
[43] F. Cui, D. Wang, F. Hu, et al., Energy Storage Mater. 44 (2022) 197–205.
[44] T. He, Y. Ye, H. Li, et al., Mater. Today 43 (2021) 53–61.
[45] S. Kim, V. Soundharrajan, S. Kim, et al., Nanomaterials 11 (2021) 1905.
[46] K. Zhu, T. Wu, K. Huang, Adv. Energy Mater. 9 (2019) 1901968.
[47] P. He, M. Yan, G. Zhang, et al., Adv. Energy Mater. 7 (2017) 1601920.
[48] N. Zhang, M. Jia, Y. Dong, et al., Adv. Funct. Mater. 29 (2019) 1807331.
[49] W. Yang, W. Yang, Y. Huang, et al., Chin. Chem. Lett. 33 (2022) 4628–4634.
[50] X. Wang, Y. Zhang, J. Zheng, et al., J. Colloid Interface Sci. 554 (2019) 191–201.
[51] Y. Zhang, H. Jiang, Q. Wang, et al., Chem. Eng. J. 352 (2018) 519–529.
[52] J. Zheng, C. Liu, M. Tian, et al., Nano Energy 70 (2020) 104519.